Check for updates

Laser & Photonics Reviews

LASER & PHOTONICS REVIEWS

www.lpr-journal.org

RESEARCH ARTICLE

Chip-Integrated Metalens for Near-Infrared Imaging With Modulated Angular Response for Stray-Light Suppression

Chunyi Niu[1] | Chen Chen[1,2] | Jiacheng Sun[1] | Xiaomin Du[1] | Junyi Wang[1] | Jian Li[1] | Shanshan Hu[1] | Wange Song[1] | Shining Zhu[1] | Din Ping Tsai[2,3,4] | Tao Li[1]

[1]National Laboratory of Solid State Microstructures, Key Laboratory of Intelligent Optical Sensing and Manipulations, Jiangsu Key Laboratory of Artificial Functional Materials, College of Engineering and Applied Sciences, Nanjing University, Nanjing, China | [2]Department of Electrical Engineering and State Key Laboratory of Terahertz and Millimeter Waves, City University of Hong Kong, Kowloon, Hong Kong SAR, China | [3]Department of Physics and State Key Laboratory of Optical Quantum Materials, City University of Hong Kong, Kowloon, Hong Kong SAR, China | [4]Shenzhen Research Institute, City University of Hong Kong, Shenzhen, China

Correspondence: Chen Chen (chenchen2021@nju.edu.cn) | Din Ping Tsai (dptsai@cityu.edu.hk) | Tao Li (taoli@nju.edu.cn)

Received: 26 June 2026 | **Revised:** 14 September 2026 | **Accepted:** 18 September 2026

Keywords: angular filtering | integrated imaging | metalens | stray-light suppression | supercells

ABSTRACT

Stray-light suppression is a fundamental requirement in a wide range of optical applications, such as astronomical observations, optical communications, high-precision sensing, and high-quality imaging. For example, conventional optical imaging systems usually rely on optical baffles to physically block stray light. However, these result in bulkiness and complexity of the system, and generally lack flexible and compact solutions for stray-light suppression. Here, we propose a new strategy based on a metalens with modulated angular responses for simultaneous stray-light suppression and wavefront modulation. Based on this dual-function design strategy, we demonstrate excellent performance in near-infrared far-field imaging, in which image quality is significantly enhanced. Moreover, a more uniform intensity distribution is achieved in flat-field imaging. Both imaging schemes are implemented directly on a CMOS sensor, offering a promising route toward image quality enhancement in compact and integrated optical systems.

1 | Introduction

Stray light is highly detrimental to high-performance optical systems, as it introduces noise, reduces signal fidelity, and generates other unwanted effects [1–11]. For instance, in infrared imaging spectrometers, stray light arising from atmospheric scattering and internal reflections can degrade imaging quality and reduce spectral resolution [1–4]. For spaceborne remote sensing, stray light originating from solar illumination and structural scattering can reduce image contrast and degrade imaging performance [5–7]. In conventional infrared optical imaging systems, stray light arises from multiple sources, including reflections and scattering within the system, as well as unwanted external light entering the system and reaching the imaging plane [8–11]. Such stray light acts as optical "noise," leading to image fogging and consequently reducing image contrast and obscuring image details. Figure 1a illustrates imaging in the presence of external stray light. The well-known veiling flare is a typical manifestation of such stray-light effects. Therefore, the ability to selectively control or suppress stray light is critical, as it can significantly affect imaging quality, detection sensitivity, and communication reliability. Here, we primarily focus on external stray light entering the imaging system at large incident angles. Conventional approaches for suppressing such stray light include mechanical baffles [12–14] and light-absorbing coatings [15, 16]. However, these approaches may introduce additional system complexity

All rights reserved, including rights for text and data mining and training of artificial intelligence technologies or similar technologies.
© 2026 Wiley-VCH GmbH.

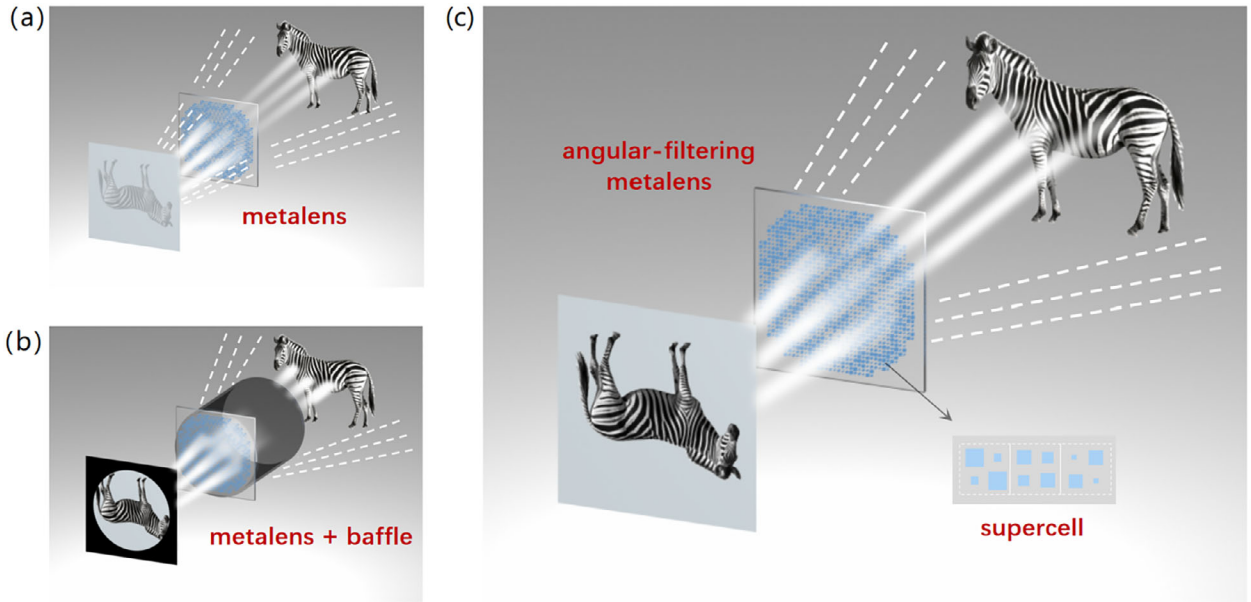


FIGURE 1 | Schematic comparison of different strategies for stray-light suppression in metalens-based imaging systems. (a) Imaging with a conventional metalens in the presence of stray light, showing reduced image contrast. (b) Imaging with the same conventional metalens equipped with a mechanical baffle, which improves image contrast at the cost of increased system size. (c) Imaging with an angular-filtering metalens under identical conditions, achieving enhanced image contrast without increasing the system size. The inset illustrates the supercell of the angular-filtering metalens. The solid lines represent the useful imaging light, while the dashed lines denote stray light.

and generally provide limited flexibility (see Figure 1b). This underscores the need for compact, versatile components that can actively filter unwanted light.

Advances in micro- and nano-optics have yielded diverse structures capable of angle-dependent transmittance modulation. In 2014, broadband angular filtering was first realized by combining photonic crystals with Brewster's effect [17]. Since then, various approaches have been developed. Narrowband angular filtering has been implemented via guided-mode resonances [18, 19] and high-Q bound states in the continuum (BICs) [20, 21]. Multilayer Bragg stacks [22, 23] exhibit angle-dependent spectral shifts, producing transmittance modulation at a fixed wavelength. In practical systems, angular-filtering microstructures have been employed to reduce rainbow artifacts in augmented-reality (AR) displays [24]. Despite their advantages in thickness and weight over conventional bulk optics, many existing angular-filtering devices primarily focus on transmittance modulation, while the simultaneous manipulation of other optical-field degrees of freedom remains challenging. Consequently, achieving more complex functionalities, particularly the simultaneous control of angle-dependent transmittance and other optical-field degrees of freedom, such as phase, often requires composite structures [25, 26] and remains a challenge.

Metasurfaces, as a new generation of planar optical devices, enable flexible and multidimensional manipulation of optical fields [27–38] through ultrathin layers of engineered nanostructures, thereby promoting the development of highly integrated optical systems. In this work, we propose a new strategy for angle-dependent transmittance engineering based on metasurfaces and incorporate this functionality into a metalens. Unlike conventional interference in multilayer films, here we introduce angle-dependent lateral interference of optical fields within the supercell (see the inset in Figure 1c) to achieve angular filtering. This approach is highly flexible, and we demonstrate various angular-filtering responses in both simulations and experiments, including angular low-pass, high-pass, and band-pass filtering. We then construct an angular-filtering phase library, enabling a metalens with angle-selective transmission and simultaneous phase modulation (see Figure 1c). The low-pass angular-filtering metalens (AFM) is used to suppress large-angle stray light in far-field imaging, while the high-pass AFM is employed in flat-field imaging. We integrate the AFMs directly onto a CMOS image sensor and compare their imaging performance with that of the conventional metalens (CM). The experimental results demonstrate that, in far-field imaging, the images obtained with the AFM exhibit an improved signal-to-noise ratio (SNR) compared with those obtained with the CM. A more uniform intensity distribution is also achieved in flat-field imaging. Our work provides a practical strategy for stray-light management in compact and integrated near-infrared imaging systems.

2 | Results

2.1 | Principle of Angular Filtering Based on Lateral Interference in a Supercell

Figure 2a illustrates the fundamental configuration of the designed dielectric supercell. A pair of staggered twin amorphous silicon (α-Si) nanopillars (meta-atoms) with a height (h) of 600 nm is arranged on a SiO_2 substrate, providing distinct phase responses while maintaining similarly high transmittance. The overall configuration exhibits centrosymmetry. For linearly polarized illumination, square nanorods with C_4 rotational symmetry

18638899, 0, Downloaded from https://onlinelibrary.wiley.com/doi/10.1002/lpor.71961 by Nanjing University, Wiley Online Library on [25/09/2026]. See the Terms and Conditions (https://onlinelibrary.wiley.com/terms-and-conditions) on Wiley Online Library for rules of use; OA articles are governed by the applicable Creative Commons License

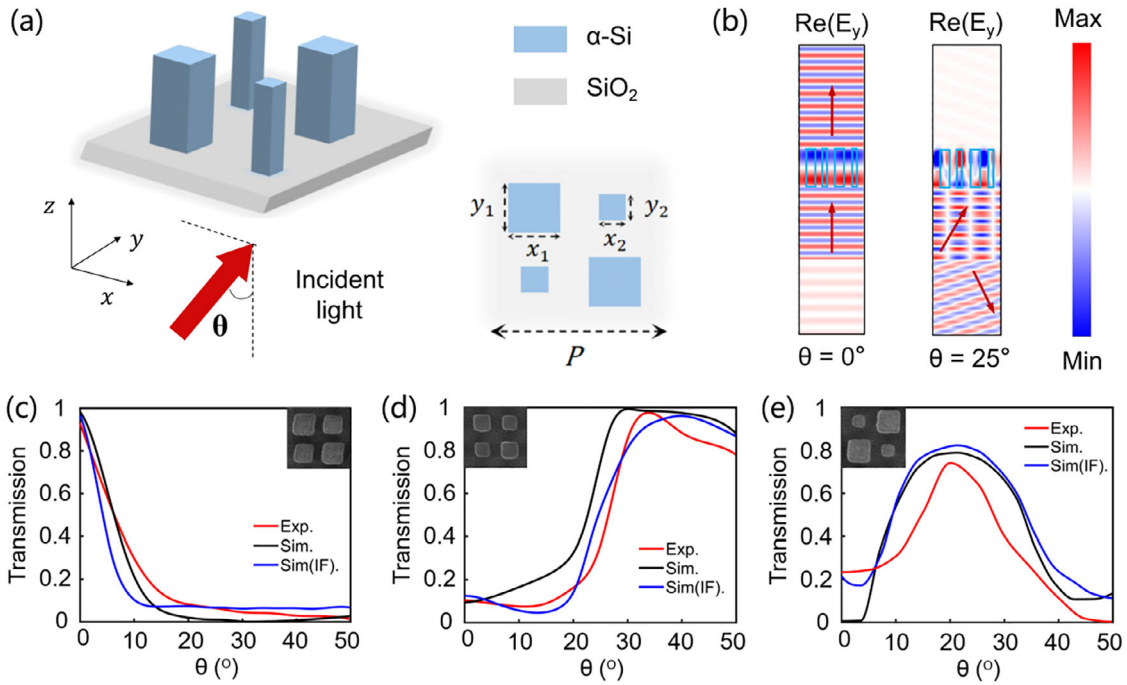


FIGURE 2 | Angular-filtering characteristics of the designed supercells. (a) Schematic of the supercell. (b) Real-part electric-field distributions of the supercell under normal incidence (0°) and oblique incidence (25°). Transmittance curves of the (c) angular low-pass, (d) high-pass, and (e) band-pass filtering metasurfaces: the measured transmittance (red curves), the simulated transmittance (black curves), and the normalized intensity calculated based on interference theory (blue curves). The insets show the corresponding SEM images.

($x_1 = y_1$ and $x_2 = y_2$) or cylinders are employed to minimize polarization conversion. The operating wavelength is set to λ = 980 nm to match the near-infrared illumination used in the imaging experiments. The supercell period is set to 800 nm to satisfy the Nyquist sampling criterion [39]. The minimum linewidth of the square nanorods is constrained to 100 nm to ensure fabrication feasibility and accuracy.

Each nanopillar can be regarded as a subwavelength dielectric waveguide, and k_0 denotes the free-space wavenumber. Under oblique incidence, an in-plane wavevector component $k_{\parallel} = k_0 \sin(\theta)$ arises, which modifies the coupling of the incident field to the optical modes supported by the nanopillar, thereby altering its transmitted amplitude and phase. The near-field distribution of the nanopillar varies with the incident angle (see Figure S1), indicating an angle-dependent modal response. This response can be described by an angle-dependent effective refractive index $n_{eff}(\theta)$. Therefore, the transmitted phase becomes angle-dependent [40, 41] and can be approximately described as

$$\varphi(\theta) = k_0\, n_{eff}(\theta)\, h \tag{1}$$

Thus, the transmitted fields of the two distinct meta-atoms can be expressed as $E_1 = A_1 \exp(i\varphi_1(\theta))$ and $E_2 = A_2 \exp(i\varphi_2(\theta))$. Assuming that both meta-atoms exhibit high transmittance, their transmitted amplitudes can be approximated as $A_1 \approx A_2 \approx 1$, the total output field resulting from collective interference can be expressed as:

$$E = 2\cos\left(\frac{\varphi_1(\theta) - \varphi_2(\theta)}{2}\right) \exp\left[i\left(\frac{\varphi_1(\theta) + \varphi_2(\theta)}{2}\right)\right] \tag{2}$$

Details can be found in Note S2. Because the phase difference between the two distinct nanopillars varies with the incident angle, the total output intensity also varies accordingly. To achieve angular low-pass filtering (i.e., high transmittance at normal incidence with suppression at oblique angles), two nanopillars with high transmittance are selected. Their phase difference is designed to be close to 0 (or 2π) at normal incidence, leading to constructive interference and thereby allowing most of the light to be transmitted. As the incident angle increases, the phase difference is designed to approach π, resulting in destructive interference in the transmitted field. Meanwhile, the suppressed transmission is accompanied by enhanced reflection, as shown in Figure 2b. Conversely, an opposite phase variation trend gives rise to an angular high-pass filtering response (i.e., high transmittance at large incident angles with reduced transmission at normal incidence). Notably, the lateral interference mechanism relies on the independent modulation of the electromagnetic field by each meta-atom. Thus, minimizing the coupling between the meta-atoms is essential. To this end, α-Si is employed due to its high refractive index, which can enhance electric field localization within individual meta-atoms. In addition, increasing the spacing between adjacent meta-atoms and selecting single-mode nanopillars [42] further suppress near-field coupling, thereby ensuring a purer interference response.

Furthermore, to efficiently design the structure, we adopt an inverse design strategy. Details can be found in Note S3. The geometry of the supercell is optimized using a particle swarm optimization algorithm to achieve the desired transmittance profiles, including low-pass, high-pass, and band-pass (i.e., selective transmission within a specific angular range). After convergence, the angle-dependent transmittances of the optimized supercell

18638899, 0, Downloaded from https://onlinelibrary.wiley.com/doi/10.1002/lpor.71961 by Nanjing University, Wiley Online Library on [25/09/2026]. See the Terms and Conditions (https://onlinelibrary.wiley.com/terms-and-conditions) on Wiley Online Library for rules of use; OA articles are governed by the applicable Creative Commons License

are obtained through finite-difference time-domain (FDTD) simulations. The corresponding phase responses of the meta-atoms are then extracted and substituted into Equation (2) to calculate the interference field, from which the interference intensity is obtained. The calculated transmittance (black curves) closely matches the normalized interference intensity (blue curves) (see Figure 2c–e), thereby supporting the proposed interference mechanism. Subsequently, the three types of structures are fabricated as 300 μm × 300 μm metasurfaces on a fused silica substrate (refractive index of 1.457 at 980 nm) by electron-beam lithography (Elionix, ELS-F125) and dry etching (Oxford Instrument, Plasma Pro100 Cobra300). The measured angle-dependent transmittance (red curves) shows good agreement with the simulated results (black curves) (see Figure 2c–e). The critical angle (θ_c), defined as the incident angle at which the transmittance decreases to 10% (for low-pass filtering) or increases to 90% (for high-pass filtering), is employed to quantify the angular filtering performance. For the optimized low-pass and high-pass structures, the corresponding θ_c values are ±12.7° and ±26.7°, respectively. To achieve more versatile control functionalities, we further investigate the tunability of θ_c. It is found that the modal field distribution of the nanopillar varies with the lattice period, and θ_c can be tuned by adjusting the period, as shown in Note S4. Moreover, the proposed angular filtering structure exhibits potential applicability in image differentiation. We experimentally demonstrated image edge enhancement using an angular high-pass filtering metasurface without relying on conventional 4*f* systems [43–47]. The experimental setup and results are presented in Note S5.

2.2 | Design of an Angular Low-Pass Metalens for Far-Field Imaging

Owing to the multidimensional optical-field manipulation capability of metasurfaces, we incorporate phase modulation into the angular-filtering supercell design, thereby enabling compact imaging systems with intrinsic stray-light suppression. Using inverse design, an eight-order propagation-phase library of low-pass filtering supercells covering 0 to 2π is constructed for linearly polarized incidence. The corresponding transmittance and phase distributions are shown in Figure 3d. For comparison, an eight-order non-filtering phase library consisting of supercells with $x_1 = x_2 = y_1 = y_2$ is constructed for the CM. The corresponding transmittance and phase distributions are shown in Figure 3a. This design achieves high transmittance within ± 60° through constructive interference and maintains the same supercell period as the filtering library, ensuring consistent phase sampling conditions for metalens design. The phase profile of the metalens is described by the hyperbolic function:

$$\varphi(x,y) = \frac{2\pi}{\lambda}\left(f - \sqrt{(x^2+y^2)+f^2}\right) \tag{3}$$

where λ = 980 nm is the design wavelength, and f is the focal length. We conducted full-wave simulations using commercial FDTD software to evaluate the focusing performance of the two metalenses under different incident angles, as shown in Note S6. A comparison reveals that the focal intensity of the AFM decreases at large incident angles, consistent with its angular filtering functionality. Subsequently, we fabricated both the CM and the AFM on a fused silica substrate for comparison. Both metalenses have a diameter of 300 μm, a numerical aperture (NA) of 0.316, and an identical phase profile. Figure 3b,e show their optical and scanning electron microscope (SEM) images, respectively. An objective lens is used to generate a wide-angle illumination condition to simulate the complex lighting environments, and the focal spots are characterized at the designed focal plane (see Figure 3f,g). The full width at half maximum (FWHM) is 2.10 μm for the CM and 1.97 μm for the AFM (the optical setup is shown in Figure S7). To evaluate their imaging performance, the modulation transfer functions (MTFs) are calculated from the measured point spread functions, as shown in Figure 3c. Due to fabrication errors [48], both MTF curves deviate from the diffraction limit. Nevertheless, the MTF of the AFM is slightly higher than that of the CM. To further determine the effective imaging field of view (FOV), we calculated the MTFs of the CM under different incident angles from 0° to 50°. As shown in Figure S7a, the effective imaging angular range of the CM is approximately −30° to +30°. Notably, the high-transmission angular range of the AFM is comparable to this effective imaging range, providing a reasonable trade-off between effective imaging performance and stray-light rejection (see Note S8).

Following the basic characterization, the imaging performances of the two metalenses are further compared. Figure 4a shows the integrated experimental setup. The metalens is mounted on a CMOS image sensor using a layer of optically clear adhesive tape (OCA, 50 μm thick), which serves as both a connector and a spacer. The sensor features a 400 μm-thick transparent cover glass, resulting in a total imaging distance of 450 μm. The light source is a planar LED with an emission bandwidth of 980 ± 10 nm. The results presented in Note S9 demonstrate that the supercell maintains distinct angular-filtering performance across this spectral range. First, we perform reflective imaging of metallic objects, which are illuminated by the light source from the side, and the metalenses collect the reflected light from the objects. Figure 4b shows the imaging results of the CM. The stray light originating from the reflections of surrounding objects reaches the imaging system at large incident angles and leads to overall image blurring. In Note S10, the calculated angular range of the useful image signal is approximately −20.7° to +20.7°, which lies within the high-transmission angular range of the AFM, whereas part of the stray light falls within the low-transmission angular range and is therefore effectively mitigated. Figure 4c shows the imaging results of the AFM under the same imaging conditions. Consequently, the image contrast is enhanced, allowing object details to be resolved more clearly. To quantitatively evaluate the imaging quality, we defined SNR = 10 $\log_{10}(I_{signal}/I_{noise})$, where I_{signal} refers to the intensity of the signal that can be clearly distinguished and I_{noise} refers to the fluctuation intensity of the background noise. Figure 4d shows the calculated SNRs at four corresponding positions (A–D) in the two imaging results. The AFM exhibits an average SNR improvement of 3.5 dB compared with the CM. Detailed calculation procedures are provided in Note S11. The proposed design also maintains its functionality under circularly polarized illumination, as demonstrated in Note S12.

To further demonstrate the improved detail-resolving capability of the AFM in the presence of stray light, we designed a finely detailed target pattern (a girl wearing hair accessories)

18638899, 0, Downloaded from https://onlinelibrary.wiley.com/doi/10.1002/lpor.71961 by Nanjing University, Wiley Online Library on [25/09/2026]. See the Terms and Conditions (https://onlinelibrary.wiley.com/terms-and-conditions) on Wiley Online Library for rules of use; OA articles are governed by the applicable Creative Commons License

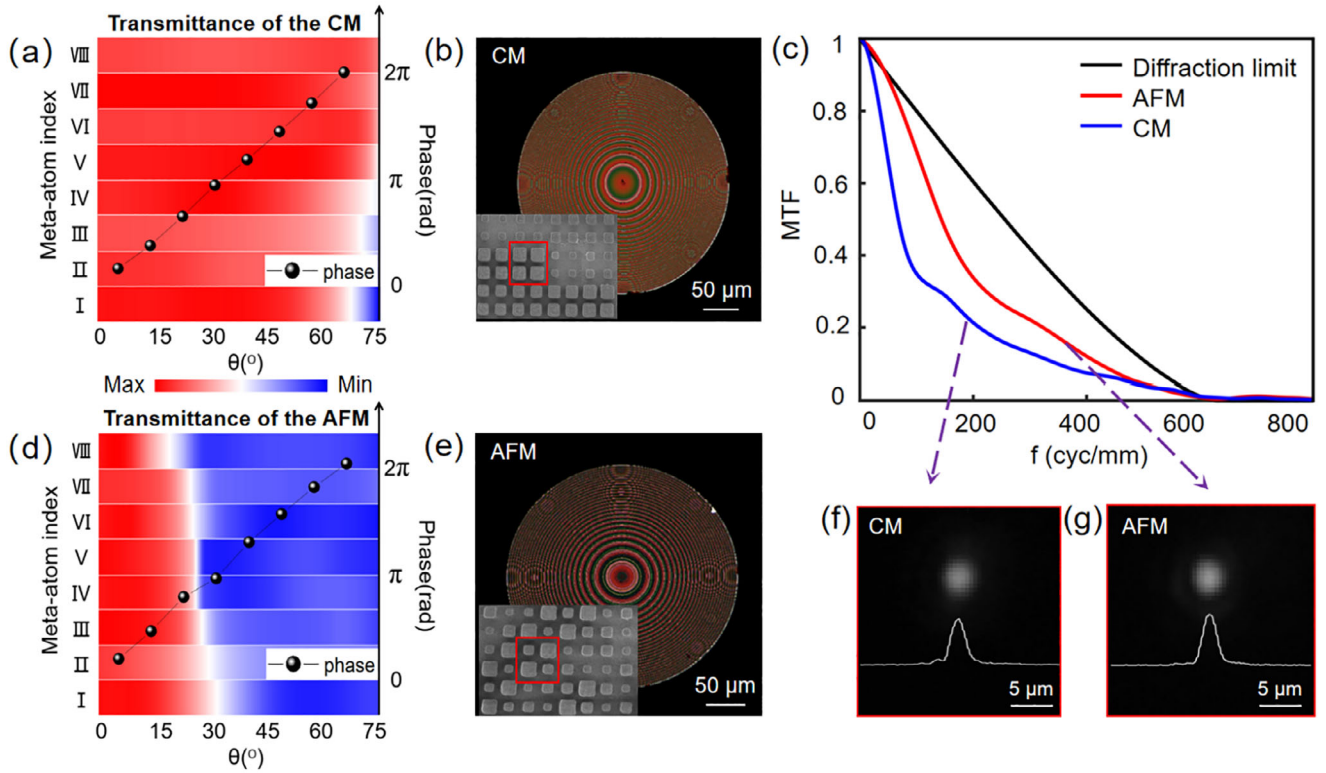


FIGURE 3 | Experimental characterization of the metalenses: (a) Transmittance and phase distributions of the supercells in the conventional phase library. (b) Optical and SEM images of the CM. (c) Measured MTFs of the CM and AFM and the diffraction-limited MTF. (d) Transmittance and phase distributions of the supercells in the low-pass angular-filtering phase library. (e) Optical and SEM images of the AFM. (f,g) Measured focal spots of the CM and AFM, respectively.

and performed transmission imaging. The experimental setup is shown in Figure 4e. The designed target image is attached to the surface of the planar LED. The angular range of the image signal, calculated in Note S10, is approximately −17.9° to +17.9°. The SMD 2835 LED chips have an emission angle of ±60°, leading to large-angle stray light during the imaging process. In the presence of such stray light, the imaging result of the CM exhibits elevated overall brightness, and the fine details are obscured (see Figure 4f). However, the imaging result of the AFM clearly resolves fine details, such as the facial features and hair accessories of the girl (see Figure 4g). To compare with the conventional approach, we kept the imaging setup unchanged and mounted a 4.5-cm-long baffle in front of the CMOS sensor. The angular-filtering performance of the baffle is quantitatively characterized in Note S13, showing that the filtering effect increases as the baffle length increases. The corresponding imaging result is shown in Figure 4h, where an improvement in image contrast can be observed due to the suppression of large-angle stray light. However, the baffle also blocks part of the light from the object edges, resulting in a loss of edge information. To avoid this loss, the imaging system, together with the baffle, needs to be positioned farther from the object, which consequently reduces the image size. These results indicate that the angular-filtering performance of a conventional baffle strongly depends on geometric parameters such as its length and position. In contrast, the AFM does not require such geometric constraints, thereby reducing the axial footprint of the imaging system.

2.3 | Design of an Angular High-Pass Metalens for Flat-Field Imaging

Flat-field imaging, as a method for high-information-content acquisition, provides a reliable basis for quantitative analysis and comparison. In conventional flat-field imaging, the central field corresponds to near-normal incidence and the edge regions correspond to oblique incidence. For a conventional metalens, the intensity distribution across the image plane is nonuniform, with lower intensity toward the edges. To enhance edge visibility and compensate for the reduced light-collection efficiency at large incident angles, the overall exposure or illumination is often increased. However, this approach can lead to overexposure in the central region, thereby causing information loss. This trade-off between enhancing edge visibility and avoiding central-region overexposure represents a key challenge in conventional flat-field imaging.

To demonstrate the flexibility of our dual-functional method, we further design a high-pass AFM for oblique incidence, which selectively modulates the transmission of light at different incident angles, thereby rebalancing the energy distribution between the central and edge regions. By suppressing low-angle light components while maintaining high transmission for high-angle components, the metalens effectively mitigates central overexposure while preserving edge visibility. In this work, the AFM is designed for an oblique incidence angle of 23°, and the corresponding light-propagation schematic is illustrated in

18638899, 0, Downloaded from https://onlinelibrary.wiley.com/doi/10.1002/lpor.71961 by Nanjing University, Wiley Online Library on [25/09/2026]. See the Terms and Conditions (https://onlinelibrary.wiley.com/terms-and-conditions) on Wiley Online Library for rules of use; OA articles are governed by the applicable Creative Commons License

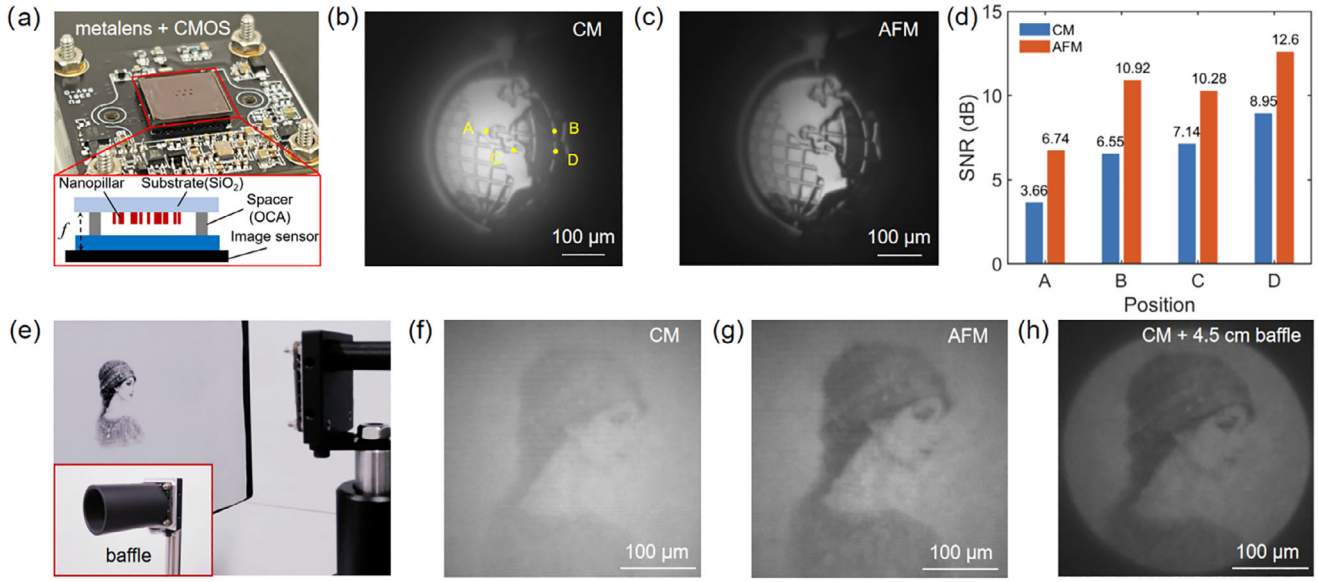


FIGURE 4 | Imaging performance of the metalenses: (a) Integrated architecture of the device. Reflective imaging results of metallic objects obtained using (b) the CM and (c) the AFM. (d) SNR comparison at different sampling positions in (b) and (c). (e) Experimental setup for transmission imaging. Transmission imaging results obtained using (f) the CM, (g) the AFM, and (h) the CM with a 4.5 cm baffle.

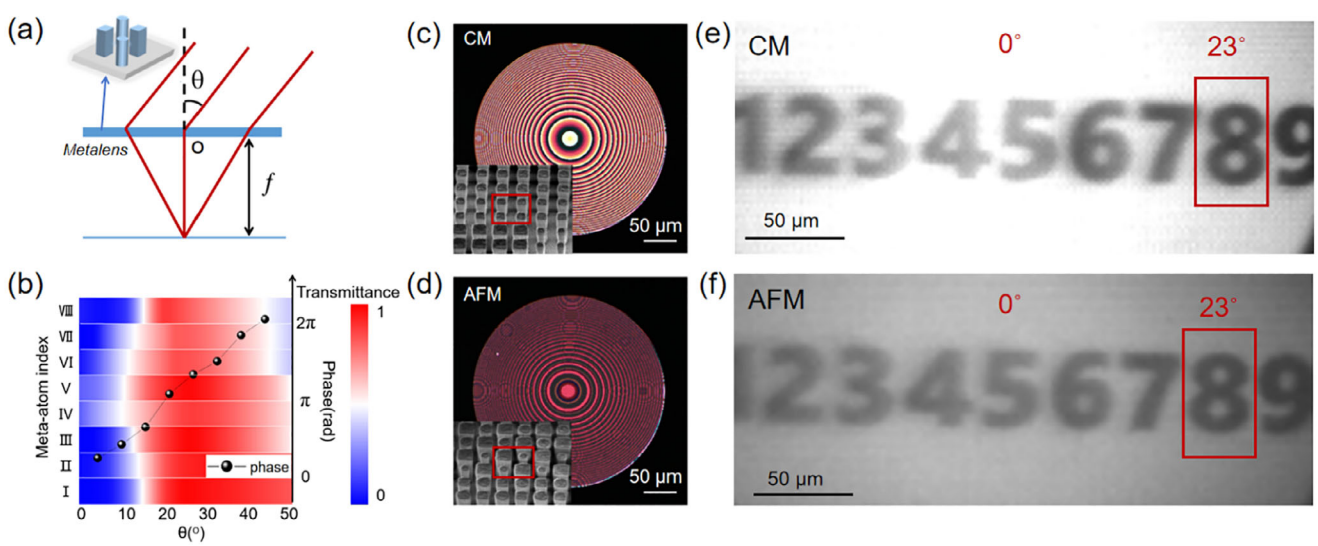


FIGURE 5 | Results of the angular high-pass metalens for flat-field imaging: (a) Schematic illustration of focusing obliquely incident light by a metalens. (b) Transmittance and phase distributions of the structures in the angular high-pass filtering phase library. (c,d) Optical and SEM images of the CM and AFM, respectively. (e,f) Imaging results obtained using the CM and AFM, respectively, showing a more uniform brightness distribution for the AFM.

Figure 5a. Since the hyperbolic phase in Equation (3) is derived for normal incidence, oblique incidence introduces additional aberrations. Therefore, we introduce phase compensation to achieve efficient focusing at the incident angle of θ:

$$\varphi\ (x,y,\theta) = \frac{2\pi}{\lambda}\left[f-\sqrt{(x-f\tan\theta)^2+y^2+f^2}-x\sin\theta\right] \quad (4)$$

To improve the design flexibility, a hybrid supercell consisting of cylinders and square prisms is adopted. We optimize an eight-order propagation-phase library. The corresponding transmittance and phase distributions are presented in Figure 5b. The supercells exhibit a high-pass angular-filtering response, with reduced transmittance at small incident angles and relatively high transmittance around the design incidence angle of 23°. In Note S14, we demonstrate the suppression of small-angle incident light by the AFM through simulations. Accordingly, the focusing efficiency also varies with the incident angle.

Similarly, we fabricated the aforementioned metalenses on fused silica substrates, each with a diameter of 300 μm and an NA of 0.316. Figure 5c,d present their optical and SEM images. In the experiment, a piece of paper printed with the digits "123456789" is placed on the LED as the imaging target, and

18638899, 0, Downloaded from https://onlinelibrary.wiley.com/doi/10.1002/lpor.71961 by Nanjing University, Wiley Online Library on [25/09/2026]. See the Terms and Conditions (https://onlinelibrary.wiley.com/terms-and-conditions) on Wiley Online Library for rules of use; OA articles are governed by the applicable Creative Commons License

the digit "8" corresponds to an incident angle of approximately 23° at the metalens. With the CM, the resulting image exhibits a non-uniform intensity distribution, with overexposure in the central region (see Figure 5e). In contrast, the image obtained with the AFM exhibits a more uniform intensity distribution (see Figure 5f). Therefore, our method provides a solution to the central field overexposure issue in flat-field imaging with a large field of view. These results highlight the potential of angle-selective metasurfaces for enhancing imaging quality in optical systems and open new opportunities for compact and multifunctional optical imaging devices.

3 | Discussion and Conclusion

In this work, we develop angle-dependent transmittance modulation via lateral angular interference within a supercell to suppress stray light in optical imaging. This angular-filtering performance is demonstrated both in numerical simulations and experimental measurements, including angular low-pass, high-pass, and band-pass filtering. We then employed the phase modulation capability of the supercells to integrate angular-filtering functionality into a metalens. Experimental imaging results show that the angular low-pass filtering metalens effectively suppresses stray light incident at large angles, thereby achieving a higher SNR and simultaneously reducing the footprint of the imaging system required by a mechanical baffle. Leveraging the flexibility of this approach, we further designed an angular high-pass filtering metalens for 23° incidence. Numerical simulations indicate that it achieves relatively high focusing efficiency at the design angle, and experimental results demonstrate that it mitigates the non-uniform intensity distribution in flat-field imaging. Moreover, our study adopts a chip-integrated imaging architecture. The simplified optical configuration reduces reflection-induced stray light within the system.

Overall, our integrated dual-functional design provides an effective strategy for simplifying optical system architectures and enhancing imaging SNR in complex environments. It shows strong potential for applications requiring stringent stray-light control, such as outdoor security surveillance, automotive vision systems, and astronomical observations, and can be further combined with optical-path-compression techniques [27, 49, 50] or extended to other spectral bands to enable more advanced integrated optical systems. Furthermore, our approach could potentially be integrated with more complex architectures, such as cascaded metasurfaces, polarization-multiplexed designs, or liquid-crystal-based optical systems, to enable dynamically tunable angular filtering [51–55].

4 | Methods

4.1 | Numerical Simulations

Numerical simulations were performed using the finite-difference time-domain (FDTD) method. The optical constants of the materials were taken from experimental measurements. For simulations of the supercells, at normal incidence, periodic boundary conditions were applied in both x and y directions, while perfectly matched layer (PML) boundary conditions were implemented in z direction. At oblique incidence, the boundary condition in x direction was replaced by bloch boundary conditions. For simulations of the metalenses, perfectly matched layer boundary conditions were applied in all directions. For propagation-phase model, the excitation source was configured as y polarized plane wave. For geometric-phase model, the excitation source was set as a right-circularly polarized plane wave.

4.2 | Sample Fabrication

The α-Si layer was deposited on the fused silica substrate using plasma-enhanced chemical vapor deposition (PECVD) to a final thickness of 600 nm. Then 200 nm PMMA A4 photoresist film is spin-coated onto the substrate and baked at 170°C for 5 min. A layer of water-soluble conductive polymer (AR-PC 5092) was spin-coated on the resist for the dissipation of E-beam charges. The device pattern was written on an electron beam resist using an E-beam writer (Elionix, ELS-F125). A 40-nm electron-beam-evaporated chromium layer was used to reverse the generated pattern with a lift-off process and was then used as a hard mask for dry etching the α-Si layer. After that, the devices transferred into HSE Series Plasma Etcher 200 and etched with C4F8 and SF6 (the flow rates of these two types of gases are 75 sccm:30 sccm). Finally, the chromium layer was removed by a stripping solution (ceric ammonium nitrate). The schematic of the sample fabrication process is shown in Note S15.

Author Contributions

Chunyi Niu: conceptualization, methodology, software, validation, Writing – original draft, visualization, investigation, Writing – review and editing. **Chen Chen:** writing – review and editing, supervision, methodology, data curation, resources, conceptualization. **Jiacheng Sun:** resources, project administration. **Xiaomin Du:** formal analysis. **Junyi Wang:** formal analysis. **Jian Li:** resources. **Shanshan Hu:** resources. **Wange Song:** formal analysis. **Shining Zhu:** supervision, project administration. **Din Ping Tsai:** supervision, writing – review and editing. **Tao Li:** supervision, writing – review and editing, project administration, resources, formal analysis.

Acknowledgements

The authors acknowledge the funding provided by National Key R&D Program of China (2024YFA1012600), National Natural Science Foundation of China (Nos. 62325504, 62305149, 62375232), University Grants Committee/Research Grants Council of the Hong Kong Special Administrative Region, China Project No. AoE/P-502/20, CRF Project: C5031-22G; C5078-24G, GRF Project: CityU11305223; CityU11300224; CityU11304925; CityU11305125, and City University of Hong Kong Project No. 9380131 and the Fundamental Research Funds for the Central Universities (No. KG202513) of Nanjing University. The authors thank Prof. Haijun Wu, Prof. Wangtao Lu, Prof. Nianyu Yi, Prof. Huangxin Chen & Prof. Huayi Wei for their helpful discussion in full wave simulatins.

Conflicts of Interest

The authors declare no conflicts of interest.

Data Availability Statement

Dataset that supports the findings of this study is available upon reasonable request.

18638899, 0, Downloaded from https://onlinelibrary.wiley.com/doi/10.1002/lpor.71961 by Nanjing University, Wiley Online Library on [25/09/2026]. See the Terms and Conditions (https://onlinelibrary.wiley.com/terms-and-conditions) on Wiley Online Library for rules of use; OA articles are governed by the applicable Creative Commons License

References

1. C. Ben, H. Shen, X. Yu, L. Meng, H. Cheng, and P. Jia, "Stray Light Analysis and Suppression for an Infrared Fourier Imaging Spectrometer," *Photonics* 11 (2024): 173, https://doi.org/10.3390/photonics11020173.

2. S. Zhou, "Optical Design of MWIR Imaging Spectrometer With a Cold Slit," *Proceedings of SPIE* 9860 (2016): 2219427, https://doi.org/10.1117/12.2219427.

3. M. Lin, R. Swanson, T. Moon, et al., "Stray Light Characterization of an InGaAs Anamorphic Hyperspectral Imager," *Optics Express* 18, no. 16 (2010): 17510–17520, https://doi.org/10.1364/OE.18.017510.

4. L. Zhao, M. Mou, Z. Wang, et al., "Research on Adjustable Cold View Field Diaphragm in Optical System With Linear Array Detector in AIMS," *Research in Astronomy and Astrophysics* 25 (2025): 025017, https://doi.org/10.1088/1674-4527/ad942a.

5. L. Wei, L. Yang, Y.-P. Fan, S.-S. Cong, and Y.-S. Wang, "Research on Stray-Light Suppression Method for Large Off-Axis Three-Mirror Anastigmatic Space Camera," *Sensors* 22, no. 13 (2022): 4772, https://doi.org/10.3390/s22134772.

6. A. Iwasaki and E. Oyama, "Correction of Stray Light and Filter Scratch Blurring for ASTER Imagery," *IEEE Transactions on Geoscience and Remote Sensing* 43, no. 12 (2005): 2763–2768, https://doi.org/10.1109/TGRS.2005.855065.

7. A. Baumgartner, C. Henning Köhler, S. Baur, R. Wachter, L. Polz, and A. Serdyuchenko, "Stray Light Calibration and Correction of EnMAP's Imaging Spectrometers," *IEEE Transactions on Geoscience and Remote Sensing* 63 (2025): 1–16, https://doi.org/10.1109/TGRS.2025.3552114.

8. A. V. Pravdivtsev and M. N. Akram, "Simulation and Assessment of Stray Light Effects in Infrared Cameras Using Non-Sequential Ray Tracing," *Infrared Physics & Technology* 60 (2013): 306–311, https://doi.org/10.1016/j.infrared.2013.05.014.

9. R. Guodong, Z. Liang, L. Weihua, Z. Yan, and P. Xiaodong, "Analysis and Suppression of Stray Radiation of Shortwave Infrared Imaging System," *Laser & Optoelectronics Progress* 52, no. 12 (2015): 122901, https://doi.org/10.3788/lop52.122901.

10. Z. Wu and X. Wang, "Stray Light Correction for Medium Wave Infrared Focal Plane Array-Based Compressive Imaging," *Optics Express* 28, no. 13 (2020): 19097–19112, https://doi.org/10.1364/OE.393368.

11. Z. Yang, X. Guo, S. Lu, et al., "Investigation of Stray Radiation Suppression in Infrared Imaging System Using a Novel Broadband and High-Absorption Ceramic Coating," *Applied Sciences* 11, no. 11 (2021): 4952, https://doi.org/10.3390/app11114952.

12. H. N. Yeon, D. K. Hong, C. Lee, et al., "Optimized Baffle Design for the Simultaneous Suppression of External and Internal Stray Light in an LWIR Catadioptric Optical Payload," *Current Optics and Photonics* 9, no. 1 (2025): 65–71, https://doi.org/10.3807/COPP.2025.9.1.65.

13. X. Zhong, Z. Su, G. Zhang, et al., "Analysis and Reduction of Solar Stray Light in the Nighttime Imaging Camera of Luojia-1 Satellite," *Sensors* 19, no. 5 (2019): 1130, https://doi.org/10.3390/s19051130.

14. P. Han, J. Guo, M. Zhang, R. Xue, G. Ren, and Y. Liu, "Stray Light Control for the Space-Agile Optical System With a Pointing Mirror," *Applied Optics* 62, no. 12 (2023): 3132–3141, https://doi.org/10.1364/AO.483427.

15. H. Wagner, V. Ripka, A. Dellith, et al., "Plasmonic Black Coatings With Broadband Absorption for Space Applications," *Journal of Vacuum Science & Technology A* 41, no. 5 (2023): 053209, https://doi.org/10.1116/6.0002821.

16. S. Zeidler, T. Akutsu, Y. Torii, and Y. Aso, "Measuring Scattering Light Distributions on High-Absorptive Surfaces for Stray-Light Reduction in Gravitational-Wave Detectors," *Optics Express* 27, no. 12 (2019): 16890–16910, https://doi.org/10.1364/OE.27.016890.

17. Y. Shen, D. Ye, I. Celanovic, S. G. Johnson, J. D. Joannopoulos, and M. Soljacic, "Optical Broadband Angular Selectivity," *Science* 343, no. 6178 (2014): 1499–1501, https://doi.org/10.1126/science.1249799.

18. Z. Zheng, D. Smirnova, G. Sanderson, et al., "Broadband Infrared Imaging Governed by Guided-Mode Resonance in Dielectric Metasurfaces," *Light: Science & Applications* 13 (2024): 249, https://doi.org/10.1038/s41377-024-01535-w.

19. M. Cotrufo, A. Arora, S. Singh, and A. Alù, "Dispersion Engineered Metasurfaces for Broadband, High-NA, High-Efficiency, Dual-Polarization Analog Image Processing," *Nature Communications* 14 (2023): 7078, https://doi.org/10.1038/s41467-023-42921-z.

20. C. Wang, R. Wang, X. Cheng, X. Hu, and C. Wang, "Passively Broadband Tunable Dual Circular Dichroism via Bound States in the Continuum in Topological Chiral Metasurface," *ACS Nano* 18, no. 29 (2024): 18922–18932, https://doi.org/10.1021/acsnano.4c01697.

21. Q. Duan, Y. Zeng, Y. Yin, et al., "Photonic Crystal Slabs With Maximal Chiroptical Response Empowered by Bound States in the Continuum," *Photonics Research* 11, no. 11 (2023): 1919–1933, https://doi.org/10.1364/PRJ.497954.

22. Q. Qian, C. Xu, and C. Wang, "All-Dielectric Polarization-Independent Optical Angular Filter," *Scientific Reports* 7 (2017): 16574, https://doi.org/10.1038/s41598-017-16837-w.

23. Y. Liu, M. Huang, Q. Chen, and D. Zhang, "Single Planar Photonic Chip With Tailored Angular Transmission for Multiple-Order Analog Spatial Differentiator," *Nature Communications* 13 (2022): 7944, https://doi.org/10.1038/s41467-022-35588-5.

24. E. Shipton, G. Calafiore, and P. Saarikko, Rainbow Reduction for Waveguide Displays, US20210157145, 2021.

25. T. Xie, F. Zhang, M. Pu, et al., "Ultrathin, Wide-Angle, and High-Resolution Meta-Imaging System via Rear-Position Wavevector Filter," *Laser & Photonics Reviews* 17, no. 12 (2023): 2300119, https://doi.org/10.1002/lpor.202300119.

26. L. Dong, W. Kong, F. Zhang, et al., "Ultra-thin Sub-Diffraction Metalens With a Wide Field-of-View for UV Focusing," *Optics Letters* 49, no. 5 (2024): 1189–1192, https://doi.org/10.1364/OL.514291.

27. C. Chen, X. Ye, J. Sun, et al., "Bifacial-Metasurface-Enabled Pancake Metalens With Polarized Space Folding," *Optica* 9, no. 12 (2022): 1314–1322, https://doi.org/10.1364/OPTICA.474650.

28. J. Ji, J. Li, Z. Wang, et al., "On-Chip Multifunctional Metasurfaces With Full-Parametric Multiplexed Jones Matrix," *Nature Communications* 15 (2024): 8271, https://doi.org/10.1038/s41467-024-52476-2.

29. J. Wang, R. Yu, X. Ye, et al., "Quantitative Phase Imaging With a Compact Meta-Microscope," *npj Nanophotonics* 1 (2024): 4, https://doi.org/10.1038/s44310-024-00007-8.

30. W. Ye, F. Zeuner, X. Li, et al., "Spin and Wavelength Multiplexed Nonlinear Metasurface Holography," *Nature Communications* 7 (2016): 11930, https://doi.org/10.1038/ncomms11930.

31. M. Liu, W. Zhu, P. Huo, et al., "Multifunctional Metasurfaces Enabled by Simultaneous and Independent Control of Phase and Amplitude for Orthogonal Polarization States," *Light: Science & Applications* 10 (2021): 107, https://doi.org/10.1038/s41377-021-00552-3.

32. I. Kim, J. Jang, G. Kim, et al., "Pixelated Bifunctional Metasurface-Driven Dynamic Vectorial Holographic Color Prints for Photonic Security Platform," *Nature Communications* 12 (2021): 3614, https://doi.org/10.1038/s41467-021-23814-5.

33. A. Javed Satti, E. Lee, I. Javed, et al., "Nearly 180° Field-of-View Metalens for Miniaturized Imaging Systems," *Laser & Photonics Reviews* 20 (2025): 00098, https://doi.org/10.1002/lpor.202500098.

34. Y. Dong, B. Zheng, F. Yang, et al., "Full-Color, Wide Field-of-View Metalens Imaging via Deep Learning," *Advanced Optical Materials* 13 (2024): 2402207, https://doi.org/10.1002/adom.202402207.

35. C. Chen, J. Wang, R. Lin, et al., "Optical Corner Detection With Azimuthal Hilbert Transform Metasurfaces," *Science Advances* 12, no. 19 (2026): aed8301, https://www.science.org/doi/10.1126/sciadv.aed8301.

18638899, 0, Downloaded from https://onlinelibrary.wiley.com/doi/10.1002/lpor.71961 by Nanjing University, Wiley Online Library on [25/09/2026]. See the Terms and Conditions (https://onlinelibrary.wiley.com/terms-and-conditions) on Wiley Online Library for rules of use; OA articles are governed by the applicable Creative Commons License

36. X. Li, H.-T. Lee, D. Han, and J. Rho, "Metasurface-Driven Sensing in Terahertz Region: Principles, Applications, Fabrication, and Challenges," *Advanced Materials Technologies* 10 (2025): 00886, https://doi.org/10.1002/admt.202500886.

37. H. Wang, H. Wang, Q. Ruan, et al., "Coloured Vortex Beams With Incoherent White Light Illumination," *Nature Nanotechnology* 18 (2023): 264–272, https://doi.org/10.1038/s41565-023-01319-0.

38. M. Pu, X. Li, X. Ma, et al., "Catenary Optics for Achromatic Generation of Perfect Optical Angular Momentum," *Science Advances* 1 (2015): 1500396, https://doi.org/10.1126/sciadv.1500396.

39. J. W. Goodman, "Chapter 2-Analysis of Two-Dimensional Signals and Systems," in *Introduction to Fourier Optics*, (McGraw-Hill, 1968).

40. S. M. Kamali, E. Arbabi, A. Arbabi, Y. Horie, M. Faraji-Dana, and A. Faraon, "Angle-Multiplexed Metasurfaces: Encoding Independent Wavefronts in a Single Metasurface Under Different Illumination Angles," *Physical Review X* 7 (2017): 041056, https://doi.org/10.1103/PhysRevX.7.041056.

41. Z. Liu, W. Feng, Y. Long, et al., "A Metasurface Beam Combiner Based on the Control of Angular Response," *Photonics* 8, no. 11 (2021): 489, https://doi.org/10.3390/photonics8110489.

42. T. Matsui and H. Iizuka, "Effect of Finite Number of Nanoblocks in Metasurface Lens Design From Bloch-Mode Perspective and Its Experimental Verification," *ACS Photonics* 7, no. 12 (2022): 3448–3455, https://doi.org/10.1021/acsphotonics.0c01346.

43. C. Jin and Y. Yang, "Transmissive Nonlocal Multilayer Thin Film Optical Filter for Image Differentiation," *Nanophotonics* 10, no. 13 (2021): 3519–3525, https://doi.org/10.1515/nanoph-2021-0313.

44. A. Ji, J.-H. Song, Q. Li, et al., "Quantitative Phase Contrast Imaging With a Nonlocal Angle-Selective Metasurface," *Nature Communications* 13 (2022): 7848, https://doi.org/10.1038/s41467-022-34197-6.

45. Y. Zhou, H. Zheng, I. I. Kravchenko, and J. Valentine, "Flat Optics for Image Differentiation," *Nature Photonics* 14 (2020): 316–323, https://doi.org/10.1038/s41566-020-0591-3.

46. W. Xue and O. D. Miller, "High-NA Optical Edge Detection via Optimized Multilayer Films," *Journal of Optics* 23 (2021): 125004, https://doi.org/10.1088/2040-8986/ac370c.

47. M. Cotrufo, S. B. Sulejman, L. Wesemann, et al., "Reconfigurable Image Processing Metasurfaces With Phase-Change Materials," *Nature Communications* 15 (2024): 4483, https://doi.org/10.1038/s41467-024-48783-3.

48. R. Lin, J. Zhou, C. Chen, and D. P. Tsai, "Challenges and Opportunities of Metalenses," *Nature Reviews Electrical Engineering* 3 (2026): 214–225, https://doi.org/10.1038/s44287-026-00276-9.

49. O. Reshef, M. P. DelMastro, K. K. M. Bearne, et al., "An Optic to Replace Space and Its Application Towards Ultra-Thin Imaging Systems," *Nature Communications* 12 (2021): 3512, https://doi.org/10.1038/s41467-021-23358-8.

50. K. Shastri, O. Reshef, R. W. Boyd, J. S. Lundeen, and F. Monticone, "To What Extent Can Space be Compressed?," in *Bandwidth Limits of Spaceplates* (Optica, 2022), https://doi.org/10.48550/arXiv.2201.11340.

51. S. Moon, J. Kim, Y. Jo, et al., "Switchable 2D–3D Display Through a Metasurface Lenticular Lens," *Nature* 652 (2026): 1181–1187, https://doi.org/10.1038/s41586-026-10318-9.

52. X. Li, X. Cai, C. Liu, et al., "Cascaded Metasurfaces Enabling Adaptive Aberration Corrections for Focus Scanning," *Opto-Electronic Advances* 7 (2024): 240085, https://doi.org/10.29026/oea.2024.240085.

53. X. Li, Y. Kim, Y. Jeon, et al., "Parallel Bright-Field and Multi-Order Edge Imaging via Wide Field-of-View Trichannel Metalens," *Opto-Electronic Advances* 9 (2026): 250306, https://doi.org/10.29026/oea.2026.250306.

54. D. Kang, H. Heo, Y. Yang, et al., "Liquid Crystal-Integrated Metasurfaces for an Active Photonic Platform," *Opto-Electronic Advances* 7 (2024): 230216, https://doi.org/10.29026/oea.2024.230216.

55. Y. Guo, S. Zhang, M. Pu, et al., "Spin-Decoupled Metasurface for Simultaneous Detection of Spin and Orbital Angular Momenta via Momentum Transformation," *Light: Science & Applications* 10 (2021): 63, https://doi.org/10.1038/s41377-021-00497-7.

Supporting Information

Additional supporting information can be found online in the Supporting Information section.

Supporting File: lpor71961-sup-0001-SuppMat.docx.

18638899, 0, Downloaded from https://onlinelibrary.wiley.com/doi/10.1002/lpor.71961 by Nanjing University, Wiley Online Library on [25/09/2026]. See the Terms and Conditions (https://onlinelibrary.wiley.com/terms-and-conditions) on Wiley Online Library for rules of use; OA articles are governed by the applicable Creative Commons License